Modeling and Analysis of Early Events in T-Lymphocyte Antigen-Activated Intracellular-Signaling Pathways

Yanan Zheng[1], Venkataramanan Balakrishnan[2], Greg Buzzard[4],

Robert Geahlen[3], Marietta Harrison[3], Ann Rundell[1*]

[1]Department of Biomedical Engineering

[2]School of Electrical and Computer Engineering

[3]Department of Medicinal Chemistry and Molecular Pharmacology

[4]Department of Mathematics

Purdue University, West Lafayette, IN 47907, USA

*Corresponding author (rundell@ecn.purdue.edu)

Abstract

The T-cell antigen-activated signaling pathway is a highly regulated intracellular biochemical system that is crucial for initiating an appropriate adaptive immune response. To improve the understanding of the complex regulatory mechanisms controlling the early events in T-cell signaling, a detailed mathematical model was developed that utilizes ordinary differential equations to describe chemical reactions of the signaling pathway. The model parameter values were constrained by experimental data on the activation of a specific signaling intermediate and indicated an initial rapid cascade of phosphorylation events followed by a comparatively slow signal downregulation. Nonlinear analysis of the model suggested that thresholding and bistability occur as a result of the embedded positive and negative feedback loops within the model. These nonlinear system properties may enhance the T-cell receptor specificity and provide sub-threshold noise filtering with switch-like behavior to ensure proper cell response. Additional analysis using a reduced second-order model led to further understanding of the observed system behavior. Moreover, the interactions between the positive and negative feedback loops enabled the model to exhibit, among a variety of other feasible dynamics, a sustained oscillation that corresponds to a stable limit cycle in the two-dimensional phase plane. Quantitative analysis in this paper has helped identify potential regulatory mechanisms in the early T-cell signaling events. This integrated approach provides a framework to quantify and discover the ensemble of interconnected T-cell antigen-activated signaling pathways from limited experimental data.

1. Introduction

The immune system is responsible for mounting a response to infection. T-lymphocytes

(T-cells) are cellular components of the immune system that mediate the adaptive immune response. Without T-cells, an organism is vulnerable to infections as evidenced by acquired immune deficiency syndrome (AIDS). To initiate an adaptive immune response, T-cells must become activated through the engagement of antigen receptors (T-cell receptors, TCRs) expressed on the cell surface. The signal initiated by receptor engagement is transduced to the cell nucleus through intracellular signaling pathways. The signaling pathways comprise a series of cascaded chemical reactions that result in the modulation of cellular functions important in directing the immune response: lymphocyte proliferation and differentiation, and cytokine secretion.

Cellular signaling pathways comprise complex and interconnected networks of biochemical reactions acting as molecular circuits that relay signals to the genetic machinery. Although many of the proteins that participate in these biochemical reactions are known, details of their interactions and regulation remain to be elucidated. The available experimental techniques limit the ability to discover all the complex interconnected biochemical pathways without assistance from systems analysis of mathematical models. Such quantitative analysis helps to extract the control structures and the myriad of interactions from experimental results, extending the utility of the data beyond that solely available through intuition. The resulting quantitative descriptions of the T-cell signaling pathways will be useful for designing treatments for diseases arising from defects in signaling pathways such as cancer, autoimmune diseases, and asthma.

A number of researchers have developed relevant mathematical models to study T-cell signaling activation. McKeithan [34], Hlavacek *et al.* [22], Chan, George, and Stark [10],

Rabinowitz *et al.* [43], Sontag [47], and Lord, Lechler, and George [32] investigated how the duration of TCR-antigen engagement influences the cellular response. The effects of receptor internalization and serial engagement have been addressed by Sousa and Carneiro [48] and Wofsy, Coombs, and Goldstein [53]. An analysis of TCR dynamics resulting from interactions with antigen presenting cells was performed by Agrawal and Linderman [3]. A more detailed model of TCR engagement by antigen to form an immunological synapse has been generated through both analytical and experimental studies by Lee *et al*. [28, 29]. In a recent review [8], Charkraborty, Dustin, and Shaw discussed the power of the dual approach of experimentation and *in silico* modeling with examples of pioneering studies in immunology. Among them, the study by Lee *et al.* [27] determined that the lack of activated TCRs in the center of the immunological synapse was due to their rapid degradation, thus explaining the absence of TCRs in what was thought to be the site of active receptor signaling. This was achieved by integrating a stochastic model of the dominant signaling protein interactions and T-cell synapse formation with focused experiments. Other models related to the T-cell signaling pathway include work by Kim *et al*. [25] on calcium flux and Chan [9] with a simplified three component model to represent early signaling events.

All of these models have proven useful for understanding aspects of T-cell activation; however none of them paid sufficient attention to the importance of the regulatory mechanisms embedded within the intracellular signaling map. Grossman and Paul [20] suggest the interplay between positive and negative feedback regulations dynamically tune the T-cell activation threshold. Herein, this paper develops a detailed deterministic model that investigates the early T-cell signaling events through a combined effort in experimentation,

modeling and nonlinear systems analysis. In particular, the focus is to recognize positive and negative feedback regulatory regimes underlying the signaling map and their quantitative and qualitative consequences on cellular responses in a detailed kinetic context.

2. Model development

A model assembled from reported interactions that reflects the current understanding of the early TCR signaling reaction scheme is shown in Fig. 1 [2, 7, 11, 16-18, 20, 37, 42, 49, 52]. The reaction scheme shown encompasses only the common events that occur upon TCR engagement prior to the divergence into multiple downstream signaling pathways. Briefly, the engagement of a TCR results in the phosphorylation (addition of phosphate groups catalyzed by kinases) to its cytoplasmic units, denoted by TCRp in Fig. 1. This phosphorylated cytoplasmic TCR unit serves as a binding site for the cytoplasmic tyrosine kinase, Zap70. Upon binding to the TCR, Zap70's kinase activity is regulated by its phosphorylation by Lck and Fyn, members of the Src family of tyrosine kinases. The activity of Src-family kinases is regulated by the removal of an inhibitory phosphate group by protein tyrosine phosphatases (PTP). Table 1 describes each signaling element and assigns a symbol for use in constructing a mathematical model. Table 2 summarizes each of the reactions primarily in terms of protein binding, phosphate group transfers, kinase and phosphatase activation.

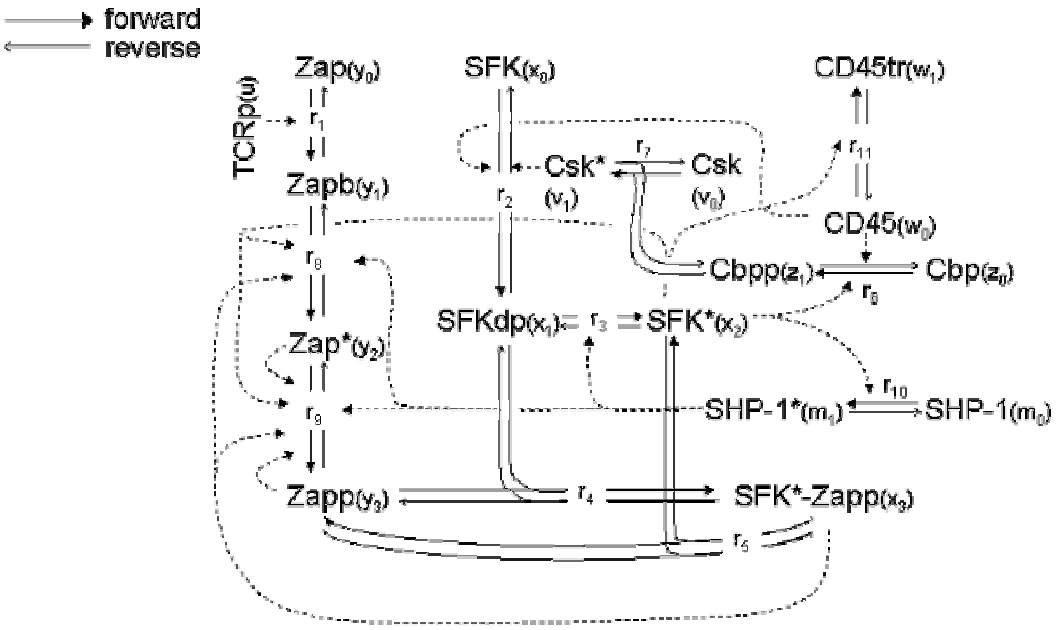

Fig. 1. Reaction scheme of early T-cell signaling events. Solid arrows denote reactions for which the forward direction is indicated; dashed arrows connect the reactions (either forward or reverse) with their catalysts.

Table 1. Summary of symbols used in the reaction scheme

Name	Symbol	Description
TCRp	u	Phosphorylated TCR-ζ chain
Zap	y_0	Protein tyrosine kinase Zap70
Zapb	y_1	Zap70 that is bound to phosphorylated receptor
Zap*	y_2	Activated Zap70 (phosphorylated at Y493 in the activation loop)
Zapp	y_3	Doubly phosphorylated Zap70 (at Y493 and Y319)
SFK	x_0	Src-family kinase (including Lck and Fyn)
SFKdp	x_1	SFK dephosphorylated at the inhibitory site
SFK*	x_2	Free fully activated SFK
SFK*-Zapp	x_3	Fully activated SFK bound to pY319 of Zap70
Cbp	z_0	Transmembrane scaffold protein Cbp
Cbpp	z_1	Tyrosine phosphorylated Cbp
Csk	v_0	Free protein tyrosine kinase Csk in the cytoplasm
Csk*	v_1	Membrane localized Csk recruited by Cbpp
CD45	w_0	Transmembrane tyrosine phosphatase CD45
CD45tr	w_1	CD45 translocated away from the receptor complex
SHP-1	m_0	Inactive tyrosine phosphatase SHP-1
SHP-1*	m_1	SHP-1 recruited to the membrane and activated

Table 2. Description of the reactions

Symbol	Description
r_1	Zap70 binding to and dissociating from phosphorylated receptor
r_2	SFK dephosphorylation by CD45 and re-phosphorylation by Csk* at the inhibitory site (Y505 in Lck, Y528 in Fyn)
r_3	SFK phosphorylation at the activation loop (Y394 in Lck,Y417 in Fyn) by autophosphorylation (or by another kinase) and dephosphorylation by PTPs including SHP-1
r_4	SFKdp binding to and dissociating from Zapp
r_5	Activated SFK releasing from and rebinding to Zapp
r_6	Cbp phosphorylation by SFK or other kinases and dephosphorylation by CD45
r_7	Csk recruitment by phosphorylated Cbp enabling its availability to SFK, and the corresponding reverse reaction
r_8	Zap70 phosphorylation at the activation loop (Y493) by activated SFK (SFK* and SFK*-Zapp) and dephosphorylation by PTPs including SHP-1
r_9	Additional Zap70 phosphorylation at Y319 by activated SFK and Zap70 and dephosphorylation by PTPs including SHP-1
r_{10}	SHP-1 activation (by SFK*) and deactivation
r_{11}	CD45 translocation away from and towards the receptors and the SFK upon T-cell activation

A mathematical model is formulated to quantitatively describe and predict the time course of kinase activation that dominates the initial signaling events, namely Src-family kinases (Lck and Fyn) and Zap70. The activation of these kinases is critical for propagation of the signal to the cell nucleus [31]. The model, coded in MATLAB, consists of 16 ordinary differential equations (ODEs) of which 10 are independent, 36 parameters, and one input signal. This model utilizes the receptor phosphorylation level (TCRp) as the system input. All reactions are modeled with first or second order kinetics. Molecular association and complex dissociation obey the rule of the Law of Mass Actions, i.e., assuming that the rate of a reaction is proportional to the product of reactant concentrations. Second-order kinetics are utilized for most enzyme-catalyzed reactions. This was derived from a simplification of the Michaelis-Menten enzyme kinetics assuming the substrate concentration is limiting. Such a

simplification contributes to minimizing the complexity of the nonlinearities and limiting the dimension of the parameter space while retaining the structure of the pathway connectivity. It is partially justified by the timing of the companion experimental data that is collected on a minute time scale, insufficient to uniquely identify detailed enzyme kinetic rate parameters. A similar representation was utilized by Heinrich, Neel, and Rapoport [21] for protein kinase/phosphatase actions in intracellular signaling pathways. For protein phosphorylation and/or dephosphorylation by enzymes not explicitly included in this model, the above expression is further reduced to first-order kinetics where the enzyme concentration becomes a constant. In addition, single molecular transitions are also governed by first order kinetics. Molecule diffusion is assumed to be rapid so no spatial information is included in the model. The differential equations and rate terms resulting from the application of these principles are stated in (1).

SFK
$$\dot{x}_0 = -\upsilon 2$$
$$\dot{x}_1 = \upsilon 2 - \upsilon 3 - \upsilon 4$$
$$\dot{x}_2 = \upsilon 3 + \upsilon 5$$

Zap70
$$\dot{x}_3 = \upsilon 4 - \upsilon 5$$
$$\dot{y}_0 = -\upsilon 1$$
$$\dot{y}_1 = \upsilon 1 - \upsilon 8$$
$$\dot{y}_2 = \upsilon 8 - \upsilon 9$$
$$\dot{y}_3 = \upsilon 9 - \upsilon 4 + \upsilon 5$$

CD45
$$\dot{w}_0 = -\upsilon 11$$
$$\dot{w}_1 = \upsilon 11$$

Csk
$$\dot{v}_0 = -\upsilon 7$$
$$\dot{v}_1 = \upsilon 7$$

Cbp
$$\dot{z}_0 = -\upsilon 6$$
$$\dot{z}_1 = \upsilon 6 - \upsilon 7$$

SHP1
$$\dot{m}_0 = -\upsilon 10$$
$$\dot{m}_1 = \upsilon 10$$

where
$$\begin{cases} \upsilon_1 = k_{1,f}(2u - y_1 - y_2 - y_3 - x_3)y_0 - k_{1,r}y_1 \\ \upsilon_2 = k_{2,f}w_0x_0 - k_{2,r}v_1x_1 \\ \upsilon_3 = k_{3,f}x_1 - (k_{3,r1}m_1 + k_{3,r2})x_2 \\ \upsilon_4 = k_{4,f}y_3x_1 - k_{4,r}x_3 \\ \upsilon_5 = k_{5,f}x_3 - k_{5,r}x_2y_3 \\ \upsilon_6 = (k_{6,f1}x_2 + k_{6,f2})z_0 - k_{6,r}w_0z_1 \\ \upsilon_7 = k_{7,f}z_1v_0 - k_{7,r}v_1 \\ \upsilon_8 = (k_{8,f1}x_2 + k_{8,f2}x_3)y_1 - (k_{8,r1}m_1 + k_{8,r2})y_2 \\ \upsilon_9 = (k_{9,f1}(y_2 + y_3 + x_3) + k_{9,f2}x_2 + k_{9,f3}x_3)y_2 - (k_{9,r1}m_1 + k_{9,r2})y_3 \\ \upsilon_{10} = k_{10,f}x_2m_0 - k_{10,r}m_1 \\ \upsilon_{11} = k_{11,f}x_2w_0 - k_{11,r}w_1 \end{cases} \quad (1)$$

It is assumed that no protein is degraded or synthesized during the time period of interest. Thus, there are six mass conservation equations, provided in (2) for SFK, Zap70, CD45, Csk, Cbp, and SHP-1, respectively.

$$\begin{aligned} x_0 + x_1 + x_2 + x_3 &= X_t \\ y_0 + y_1 + y_2 + y_3 + x_3 &= Y_t \\ w_0 + w_1 &= W_t \\ v_0 + v_1 &= V_t \\ z_0 + z_1 + v_1 &= Z_t \\ m_0 + m_1 &= M_t \end{aligned} \quad (2)$$

An example of a typical state variable differential equation is provided in (3) for free fully activated SFK where the rate terms reflect the activation of SFKdp to SFKF* ($k_{3,f}x_1$), SFK*'s inactivation by SHP-1* ($k_{3,r1}m_1x_2$), its inactivation by other PTPs ($k_{3,r2}x_2$), dissociation from Zapp ($k_{5,f}x_3$), and re-association with Zapp ($k_{5,r}x_2y_3$) respectively.

$$\dot{x}_2 = \upsilon_3 + \upsilon_5 = k_{3,f}x_1 - (k_{3,r1}m_1 + k_{3,r2})x_2 + k_{5,f}x_3 - k_{5,r}x_2y_3 \quad (3)$$

3. Model simulation and comparison to experimental data

To evaluate the model structure and constrain the parameter values, experiments were conducted to obtain a time course of Zap70 activation for comparison with the simulation results. Zap70 activation upon TCR engagement was measured in Jurkat E6.1 T-cells (2×10^7 cells/ml), stimulated at 37°C for up to 2 hours with anti-CD3 antibody UTCH1 at 2 μg/ml. After the indicated time, the cells were lysed with NP40 lysis buffer containing 1mM Na_3VO_4 and 1mM NaF to inhibit phosphatase activities. Nuclei were removed by centrifugation at $12{,}700 \times$ g. Cell lysates were processed by immunoblotting with a phospho-specific antibody against Zap70 phosphorylated at Y319 and detected by enhanced chemiluminescence. To eliminate possible Erk feedback to Lck [49], the cells were preincubated with the Mek inhibitor U0126 (2 μg/ml) at 37°C for 30 minutes. Densitometric measurements of the immunoblot films were performed using NIH software ImageJ.

Model simulations were conducted with MATLAB ODE solver 'ode15s' with the relative integration tolerance of 1e-3, which was shown to be sufficient to obtain accurate time course results. The parameters used to simulate the model were constrained by experimental measurements, observations and related mathematical models in literature as described in Table 3. The exact values of the 29 reaction rate parameters were manually tuned to fit the timing of the initial peak and decay and the maximal activation level by visual inspection.

The model simulations compare favorably to the obtained experimental data as shown in Fig. 2. The ordinate of this figure is computed as $100\times\frac{y_3 + x_3}{Y_t}$., which corresponds to the

total percentage of Zap70 phosphorylated at Y319. As the experimental antibody concentration was in excess of the amount of TCRs, the model simulations assume a constant input signal (TCRp). With the current parameter set, the model was not able to capture the second rising phase in the data, although it successfully predicted a damped response that has been consistently observed throughout all experiments. As this model captures only the early signaling events, the validity of the model at longer time periods is unknown. The second rising phase of the experimental data may be due to downstream protein synthesis, not incorporated in this model but currently under investigation.

Table 3. Parameters

Parameter Values	Description	Source
Y_t = 1e5; X_t = 1.2e5; V_t = 5e4; Z_t = 5e4; W_t = 1e5; M_t = 1e6; $[TCR]_t$ = 1e5.	Total numbers of protein copies per cell (number/cell, abbreviated as #/cell herein)	Total SFK (X_t) refer to [40]; total TCR refer to [19]; others are estimated based on relative abundances.
u = 2e4 #/cell	Number of phosphorylated receptor (input signal)	Assume 10% of total TCR is phosphorylated.
$k_{1,f}$ = 2e-5 cell/(#·s) $k_{1,r}$ = 4.2e-2 s^{-1}	Association/dissociation rate constants for Zap70–phospho-TCRζ binding	Correspond to K_D = 7nM [a] that is within the range of measured K_D for Zap70 SH2–TCRζ pITAM2,3 (higher affinity pITAMs) binding [26, 41].
$k_{4,f}$ = 5e-6 cell/(#·s); $k_{4,r}$ = 8e-3 s^{-1} $k_{5,r}$ = 1e-6 cell/(#·s); $k_{5,f}$ = 8e-2 s^{-1} $k_{7,f}$ = 8.89e-7 cell/(#·s); $k_{7,r}$ = 4e-2 s^{-1}	Association/dissociation rate constants for SFK/Csk's binding to phosphorylated Zap70/Cbp via their SH2 domains.	The correspondent K_Ds are consistent with those measured for a variety of SH2-bearing proteins to their target phospho-peptide sequences. These values ranges from the order of 1 to 1e2 nM [41].
$k_{2,r}$ = 4e-6 cell/(#·s) $k_{6,f1}$ = 0.833e-6 cell/(#·s) $k_{8,f1}$ = $k_{9,f2}$ = 0.833e-6 cell/(#·s) $k_{8,f2}$ = $k_{9,f3}$ = 2.5e-6 cell/(#·s) $k_{9,f1}$ = 4.44e-6 cell/(#·s)	Second-order rate constants for the tyrosine phosphorylation of proteins by activated kinases Zap, SFK or Csk	Consistent with the range of values used in literatures [5, 6, 45] for a variety of tyrosine kinases including PKC, MAPK and Shc, spanning from the order of 1e-7 to 1e-4 cell/(#·s) [a, b].
$k_{3,f}$ = 4e-3 s^{-1} $k_{6,f2}$ = 1e-2 s^{-1}	First-order rate constants for protein phosphorylation by other kinases	Estimated based on the correspondent second-order rate constants and the assumptions on the abundance of the responsible kinases [c] (1e3~1e4 #/cell).
$k_{2,f}$ = 4e-7 cell/(#·s) $k_{6,r}$ = 8e-7 cell/(#·s) $k_{3,r1}$ = $k_{8,r1}$ = $k_{9,r1}$ = 4e-6 cell/(#·s)	Second-order rate constants for protein dephosphorylation by CD45 or activated SHP-1	These values are within the range of the first order rate constants (second order rate constants are converted with maximal CD45 or SHP-1 activation [c]) used in literatures for the dephosphorylation of FCεRI receptor (20 s^{-1}) [14] and Shc (0.05 s^{-1} [b]) [6].
$k_{3,r2}$ = $k_{8,r2}$ = $k_{9,r2}$ = 8e-2 s^{-1}	First-order rate constants for protein dephosphorylation by other PTPs	
$k_{11,f}$ = 4e-8 cell/(#·s) $k_{11,r}$ = 2e-4 s^{-1}	CD45 translocation	CD45 translocation is observed ~20 minutes after T-cell stimulation [16].
$k_{10,f}$ = 8.64e-10 cell/(#·s) $k_{10,r}$ = 4e-4 s^{-1}	SHP-1 activation and deactivation	Estimated by fitting to the experimental data as shown in Fig. 2.

[a] For unit conversion, assume a cell volume of 5e-13L, consistent with a normal T-cell diameter of 8-10μm [1].

[b] To convert Michaelis-Menten parameters $\left(E + S \underset{k_{-1}}{\overset{k_1}{\longleftrightarrow}} ES \xrightarrow{k_p} E + P\right)$ to the second/first-order rate constants used in this paper, assume the substrate concentration << K_m, then $k_{2nd\text{-}order} \approx k_p/K_m$ and $k_{1st\text{-}order} \approx V_{max}/K_m$, where $K_m=(k_{-1}+k_p)/k_1$, $V_{max}=k_p[E]_{tot}$.

[c] Conversion between first and second order kinetics constants: $k_{1st\text{-}order}= k_{2nd\text{-}order}\times[E]$.

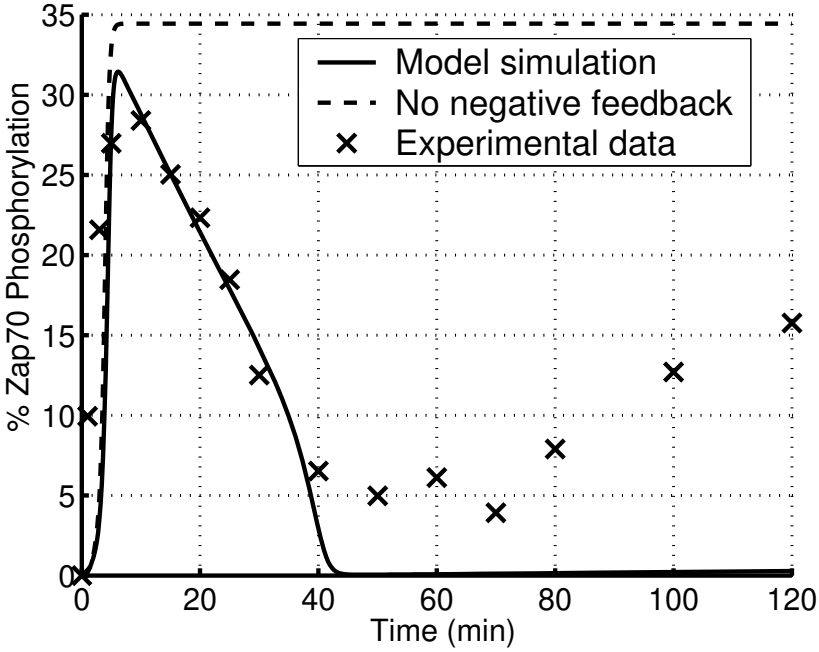

Fig. 2. Model simulations with comparison to experimental data. Elimination of the negative feedback loops was achieved with $k_{6,f1}=k_{11,f}=k_{10,f}=0$. All other parameters are the same as in Table 3. Y axis $(100\times(y_3+x_3)/Y_t)$ is the percentage of Zap70 phosphorylated at Y319, referred to as % Zap70 Phosphorylation hereafter.

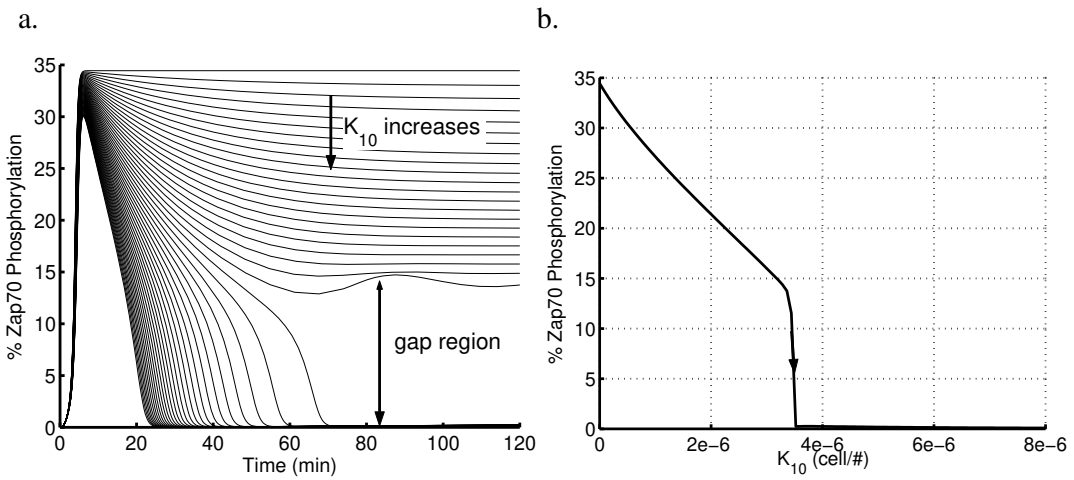

Fig. 3. Increasing negative feedback strength increases the damping. CD45-Csk feedback is eliminated ($k_{6,f1}=k_{11,f}=0$) and K_{10} varies from 0 to 8e-6 cell/# by changing $k_{10,f}$. Other parameters are the same as in Table 3. a. Model simulation results. b. Changes in the steady state of the system with increasing K_{10}.

4. Feedback regulation

In the model, the pathway regulations are reflected in several feedback loops, in which a downstream pathway product serves to modulate upstream signaling events. Such a feedback loop is positive when the modulation enhances signal propagation through the pathway, whereas a negative feedback loop will inhibit it. Two negative feedback regulation loops were considered in the model: (i) inhibition of Zap70 and SFK by SHP-1 activation [17, 49, 52] (through reactions r_{10}, r_3, r_8 and r_9 in Fig. 1), herein referred to as the SHP-1 feedback; (ii) inhibition of SFK activation through CD45 translocation [16] and Csk recruitment [7, 11] (r_2, r_6, r_7, and r_{11}), herein referred to as the CD45-Csk feedback. In addition, a positive feedback results from enhanced SFK function when bound to the doubly phosphorylated Zap70 (r_4, r_5) as evidenced by increased receptor phosphorylation and Zap70 activation [2, 42].

The model implies that the negative feedback loops play an important role in signal downregulation as without them the response is sustained (Fig. 2). The role of SHP-1 feedback loop strength was investigated by modifying the ratio of the forward and reverse rate constants associated with SHP-1 activation ($K_{10}=k_{10,f}/k_{10,r}$). Fig. 3 illustrates an increasingly damped response with increasing K_{10}. As anticipated, modulating the CD45-Csk negative feedback strength by changing the ratio of the forward and reverse rate constants associated with CD45 translocation ($K_{11}=k_{11,f}/k_{11,r}$) has similar results (data not shown). Contributions from the positive feedback loop are discussed in Section 7.

5. Switch-like behavior of the model

Interestingly, Fig. 3a demonstrated a gap region where small variations in the negative feedback strength cause a switch in the equilibrium level of the model. As shown in Fig. 3b, a threshold exists for which the negative feedback strength becomes sufficient large to damp out the sustained response. Below this threshold value, the negative feedback strength causes the equilibrium response to change proportionally.

Such switch-like behavior is also seen with variations of the input level, TCRp, implying the input signal must exceed a threshold to acquire detectable responses (Fig. 4). When the input exceeds the threshold, the response increases proportionally until it saturates. Fig. 4 also indicates that a larger threshold value is required for sustaining rather than initiating the early T-cell signaling events.

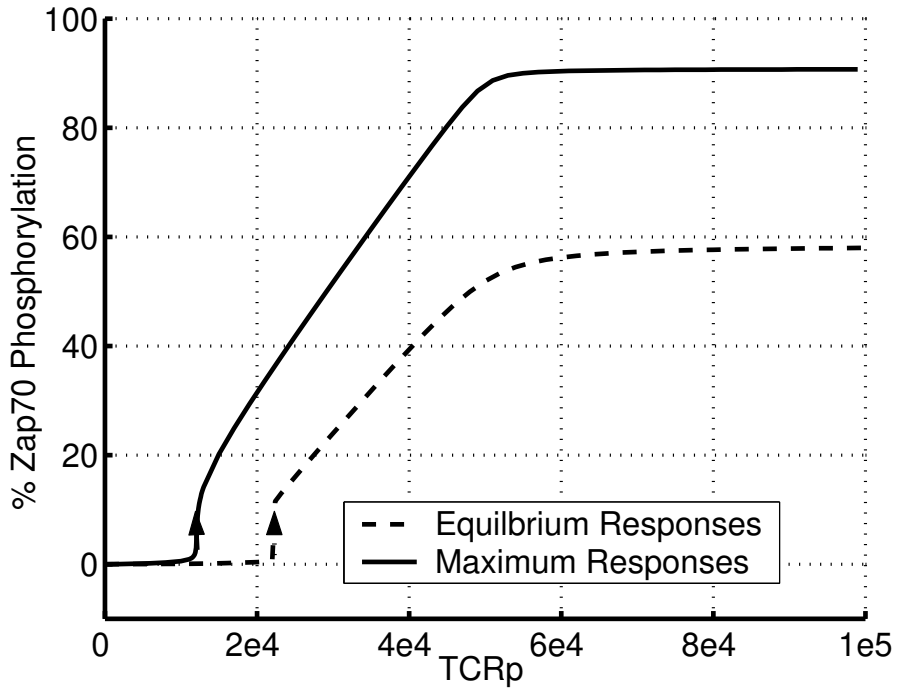

Fig. 4. Changes in the response of the system with varying input signal. Amount of TCRp (u) is varying between 0 and 1e5 (100% receptor phosphorylation), other parameters are the same as in Table 3.

6. Generation of equilibrium continuation curve

The switch-like behavior in the equilibrium state of the system shown in Fig. 3b and 4 suggest that by changing model parameters or input stimulus, the system may switch between different families of steady states, indicating the potential presence of bifurcation at the switch point. To further examine this hypothesis and explain the observed simulation dynamics, an analytical solution to the singular points of the model was obtained to inspect the continuation of the equilibrium states with varying parameters.

At equilibrium all of the derivatives of the state variables are zero which defines conditions on the rate terms (υ_i): $\upsilon_1=\upsilon_2=\upsilon_6=\upsilon_7=\upsilon_8=\upsilon_9=\upsilon_{10}=\upsilon_{11}=0$ and $-\upsilon_3=\upsilon_4=\upsilon_5$. Supplementing these with the 6 mass conservation equations, the analytical solution to the system's equilibrium states is specified by these 16 equations of 16 variables. The direct numerical solution of such coupled, high-order nonlinear equations can be a daunting task especially when multiple roots could exist. Instead, the 16 equations are reduced to 3 by explicitly expressing the rest of the state variables as functions of three "basic" variables: y_3 (Zapp), m_1 (SHP-1*), and $r \equiv w_0/v_1$ (CD45/Csk*). The resulting equations are presented in (4), (5) and (6) (see Appendix for derivation).

$$\left(y_3 + \hat{y}_2 + \hat{x}_3 + \frac{k_{9,f2}}{k_{9,f1}}\hat{x}_2 + \frac{k_{9,f3}}{k_{9,f1}}\hat{x}_3 \right)\hat{y}_2 - \frac{\left(m_1 k_{9,r1} + k_{9,r2}\right)y_3}{k_{9,f1}} = 0 \tag{4}$$

$$M_t - m_1 = \frac{m_1}{K_{10}\hat{x}_2} \tag{5}$$

$$\hat{w}_0 = \frac{W_t - \hat{w}_0}{K_{11}\hat{x}_2} \tag{6}$$

where $\hat{x}_2$, $\hat{x}_3$, $\hat{y}_2$, and $\hat{w}_0$ are equilibrium values of x_2, x_3, y_2 and w_0 as functions of y_3, m_1

and r as defined in the Appendix. The equilibrium values of all the remaining variables can also be expressed as functions of the three 'basic' variables as shown in the Appendix. Therefore, once the equilibrium values for y_3, m_1 and r are solved from (4), (5) and (6), the equilibrium states of the system are fully specified.

Eliminating either one of the negative feedback loops simplifies the solution to (4), (5), and (6) and enables the investigation of the continuation of the equilibrium states with changes in the negative feedback strength.

(i) No CD45-Csk feedback:

The CD45-Csk feedback is removed when the SFK* does not lead to the recruitment of Csk ($k_{6,f1}$=0) and translocation of CD45 ($k_{11,f}$=0). Under these conditions, (6) is uncoupled and gives $\hat{w}_0 = W_t$, then r can be solved from Appendix equation (2a) as a constant (R). With constant R, (4) and (5) define two curves on the y_3-m_1 plane whose intersection specifies the equilibrium values of y_3 and m_1. Changing K_{10} shifts the curve corresponding to (5) and hence the movement of the intersection point along the curve of (4). In order to obtain analytical equilibrium solutions with varying K_{10}, (4) is solved numerically for m_1 at fixed y_3 values using MATLAB function solver 'fsolve' with an optimization tolerance of 1e-4. Then for each (y_3, m_1) pair defined by the solution of (4), K_{10} can be computed using (5) and %Zap70 phosphorylation using derivations in the Appendix. The equilibrium continuation curve, shown in Fig. 5, indicates the corresponding steady-state %Zap70 phosphorylation with respect to K_{10}.

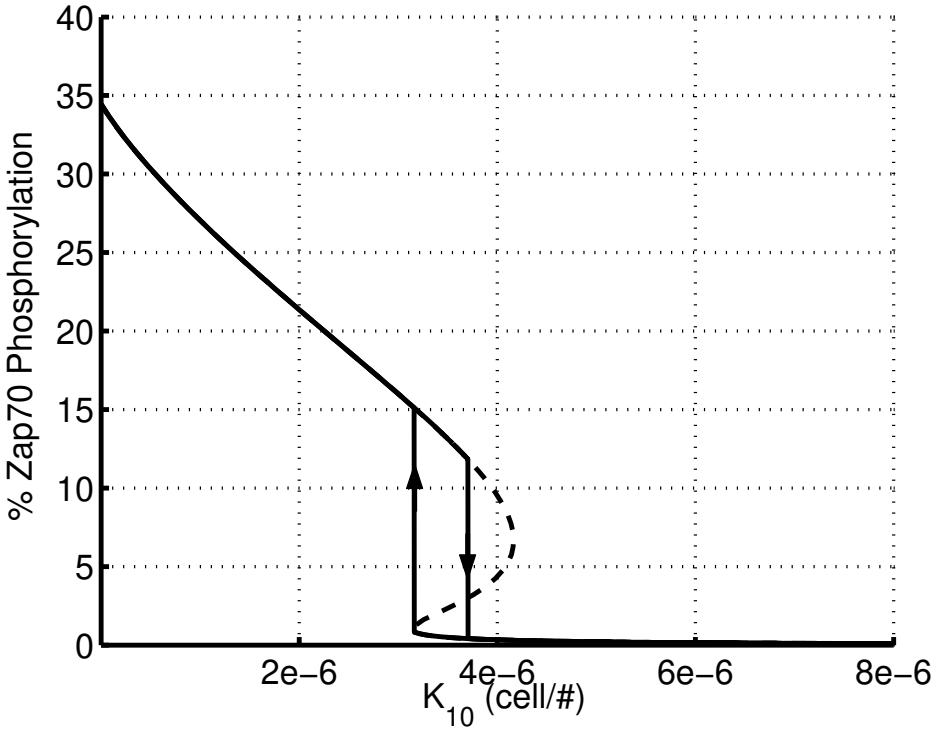

Fig. 5. The equilibrium continuation curve with varying K_{10}, as determined by numerical solution of equilibrium states, is provided by the dashed line. Solid lines indicate the variations in the steady state obtained from model time course simulations by gradually increasing or decreasing K_{10} with a step size of 8e-8 taken far from and 1.6e-9 around the switch points. The system exhibits hysteresis. The dashed line is entirely hidden by the hysteresis curve in the upper and lower branches while the visible dashed intermediate branch suggests unstable solutions. Parameters are the same as those used in Fig. 3.

Comparing Fig. 5 to the time course simulation results in Fig. 3 implies the gap region results from a switch from the upper branch of the equilibrium continuation curve to the lower one. Moving the system along the lower branch (with gradually decreasing K_{10}) eventually leads to a switch back to the upper branch. As the switch points are not equivalent for increasing and decreasing K_{10}, this system exhibits hysteresis. These results imply that the region between the two switch points (the intermediate branch of the curve) corresponds to unstable equilibrium. Thus the switch points may be bifurcation points where an equilibrium branch turns from stable to unstable. Therefore, this analysis provides insight into the

switch-like behavior of the system by revealing the possible the existence of bifurcation; although its complete verification requires a bifurcation analysis, which can be performed with professional software such as AUTO [12]. In Section 8, analysis of a reduced-order model renders partial theoretical basis for the proposed changes in the system's stability with varying negative feedback strength.

(ii) No SHP-1 feedback:

In this case, the negative feedback is removed assuming the SFK* does not activate SHP-1 ($k_{10,f}$=0). Under this condition, (5) is uncoupled and gives m_1=0. Similarly for each pair of y_3 and r determined by (4), K_{11} can be calculated from (6) with w_0 solved from (2a). The generated continuation curve is very similar to that of K_{10} in Fig. 5 (and hence not shown).

7. Impact from the positive feedback loop

The analysis in Section 6 suggests that under certain conditions, the system can have two stable steady states: one with a high activation level, and the other with a low activation level. Such bistability usually happens with positive feedback. In this model, such a positive feedback results from the enhanced SFK activity when bound to doubly phosphorylated Zap70. Therefore, the system can reside either in a state where both SFK and Zap70 are highly activated, or a state when both are weakly activated. One of the parameters dictating the strength of this positive feedback is the activity of the bound form of activated SFK (SFK*-Zapp) relative to free activated SFK (SFK*): $\alpha=k_{8,f2}/k_{8,f1}=k_{9,f3}/k_{9,f2}$. Using a procedure similar to that used to construct Fig. 5, a family of equilibrium continuation curves of K_{10} with varying α is shown in Fig. 6 (α was initially set to be three). This figure

demonstrates that the range over which the bistability occurs changes dramatically with α and even disappears when α drops below a critical value between 1 and 2 (in which case, the system has only one singular point with any K_{10} value).

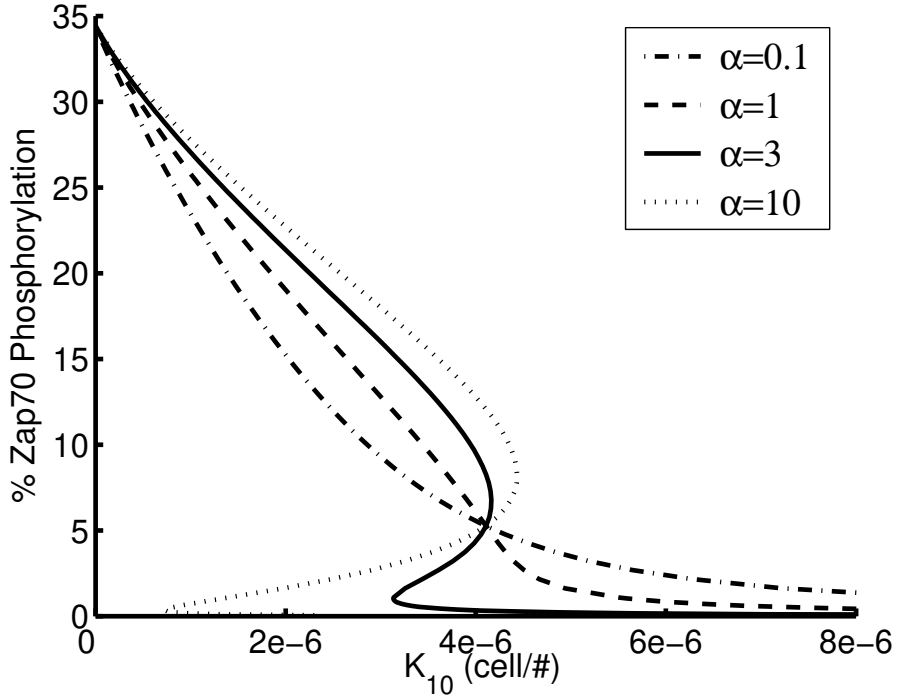

Fig. 6. The equilibrium continuation curves with varying K_{10} at different α values as determined by numerical solution of equilibrium states. $k_{8,f1}=1/(1+\alpha)\times (k^0_{8,f1}+ k^0_{8,f2})$, $k_{8,f2}=\alpha\times k_{8,f1}$, where $k^0_{8,f1}$ and $k^0_{8,f2}$ are the original parameter values in Table 3. Other parameters are the same as those used in Fig. 3.

Interestingly, with some values of α that cause the bistability to disappear, the presence of the positive feedback loop can lead to the generation of a sustained oscillation that occurs within an intermediate range of values of the negative feedback strength. The transitions between sustained, oscillatory, and damped time course responses are illustrated in Fig. 7 for selected values of K_{10}, a similar result exists for K_{11}. As really small values of α make the positive feedback negligible and the system responds gradually to variations in the negative feedback strength, these transitions between response types only happen for an intermediate

range of α. With these intermediate α values, the observed transitions between non-oscillatory and oscillatory responses in Fig. 7 may be explained by the alternation of the only singular point of the system between stable and unstable. The construction of a reduced 2nd order model will help to further explore the origin of this behavior.

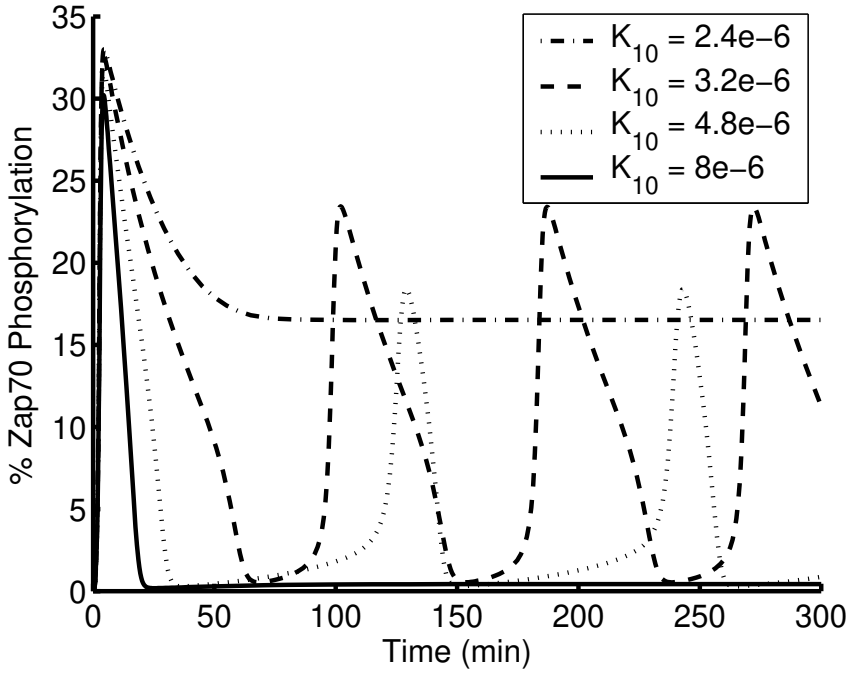

Fig. 7. Model simulations with α=1show the existence of sustained oscillations with intermediate values of K_{10}. Other parameters are the same as in Table 3.

8. Reduced 2nd order model

As high order nonlinear systems are unwieldy, it is desirable to attempt to reduce the order of the model to second order. This reduced order model will facilitate further analysis and insight into the dominant regulatory principles embedded within the early signaling events.

From the previous analysis, the two negative feedback loops serve nearly identical roles in the full model. Without loss of generality one of the negative feedback loops can be eliminated to reduce the model to a 2nd order model by setting $k_{6,f1}= k_{11,f}=0$ to eliminate the

recruitment of Csk and translocation of CD45. (In this case, the CD45-Csk feedback is eliminated.) The signal downregulation by SHP-1 activation is slow compared to the fast signal propagation through Zap70 and SFK activation ($k_{10,f} << k_{9,f1}$ or $k_{4,f}$ in Table 3). Based on the existence of these two distinct time scales in the system, the reduced-order model assumes that everything except for Zapp (y_3) and SHP-1* (m_1) (and the complementary Zap* and SHP-1) are always at quasi-steady state. By assuming all of the rapid reactions are in a quasi-steady state with changes in Zapp (y_3) and SHP-1* (m_1), the derivatives of y_3 and m_1 are fully defined by (7) and (8) which originated from the full model (1):

$$\frac{dy_3}{dt} = (k_{9,f1}(\hat{y}_2 + y_3 + \hat{x}_3) + k_{9,f2}\hat{x}_2 + k_{9,f3}\hat{x}_3)\hat{y}_2 - (m_1 k_{9,r1} + k_{9,r2})y_3 - k_{4,f}\hat{x}_1 y_3 + k_{4,r}\hat{x}_3 - k_{5,r}\hat{x}_2 y_3 + k_{5,f}\hat{x}_3 \quad (7)$$

$$\frac{dm_1}{dt} = k_{10,f}\hat{x}_2(M_t - m_1) - k_{10,r}m_1 \quad (8)$$

where the quasi-steady state values of all of the other participating chemical species, $\hat{x}_i\ (i = 0,1,2,3)$ and $\hat{y}_i\ (i = 0,1,2)$, are defined in the Appendix as functions of y_3, m_1 and r. The functional definitions of these quasi-steady states in the Appendix are derived from their corresponding differential equations being set to zero as well as the mass conservation equations as in Section 6. Recall, with the elimination of the Csk-CD45 feedback, r is a constant value (=R). Hence the 2nd order model is fully characterized by these two equations.

Although the responses obtained from the reduced model differs from that of the original model in the scaling of the time axis, some general features are preserved: this includes the damped response in the case of large α values and the self-sustained oscillation with smaller α values (compare insets of Fig. 8a and b with correspondent curves in Fig. 3a and Fig. 7, respectively). In order to understand the observed dynamics, the stability of the 2nd order

system was analyzed by linearizing it around the equilibrium points and computing the associated eigenvalues to determine their stability. These equilibrium points were identified by the intersection of the nullclines for (7) and (8) as shown in Fig. 8a and b. With varying K_{10} values, the m_1 nullcline will shift and intersect with the y_3 nullcline at different equilibrium points. Among those, the unstable equilibrium points are computed and indicated by the dashed portion of the y_3 nullcline.

The presence of this unstable branch leads to the two distinct time course responses of the model with different α values as seen previously. For large values of α, the phase plane trajectory corresponding to the inset time course shows it stabilizes at one of the 3 equilibrium points, giving rise to the damped response (Fig. 8a). The computed unstable region coincides with the dashed branch in Fig. 5, suggesting the observed switches in the full model behavior happens at the bifurcation points that separates stable from unstable equilibrium states. For smaller α, sustained oscillation occurs as the trajectory is attracted to a stable limit cycle surrounding the only unstable equilibrium point (Fig. 8b). When the changes in K_{10} value causes the intersection between the two nullclines to enter the stable region, a switch between oscillatory and non-oscillatory responses will happen as previously seen in Fig. 7 with the full model.

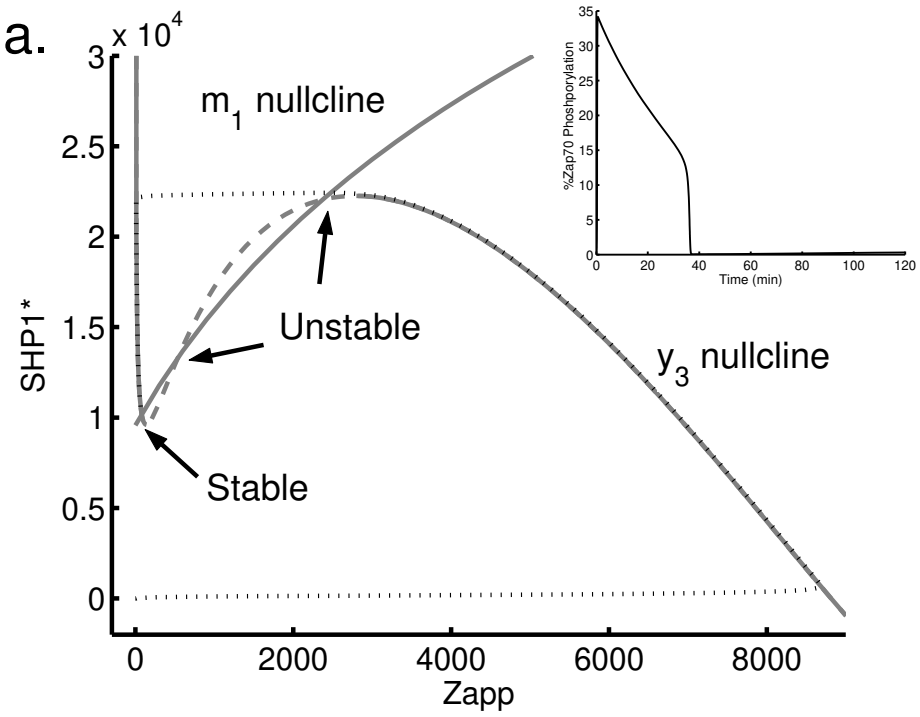
a.
x 10^4
3
2.5
2
1.5
1
0.5
0
SHP1*
m1 nullcline
Unstable
Stable
y3 nullcline
0
2000
4000
6000
8000
Zapp
%Zap70 Phoshporylation
35
30
25
20
15
10
5
0
0
20
40
60
80
100
120
Time (min)

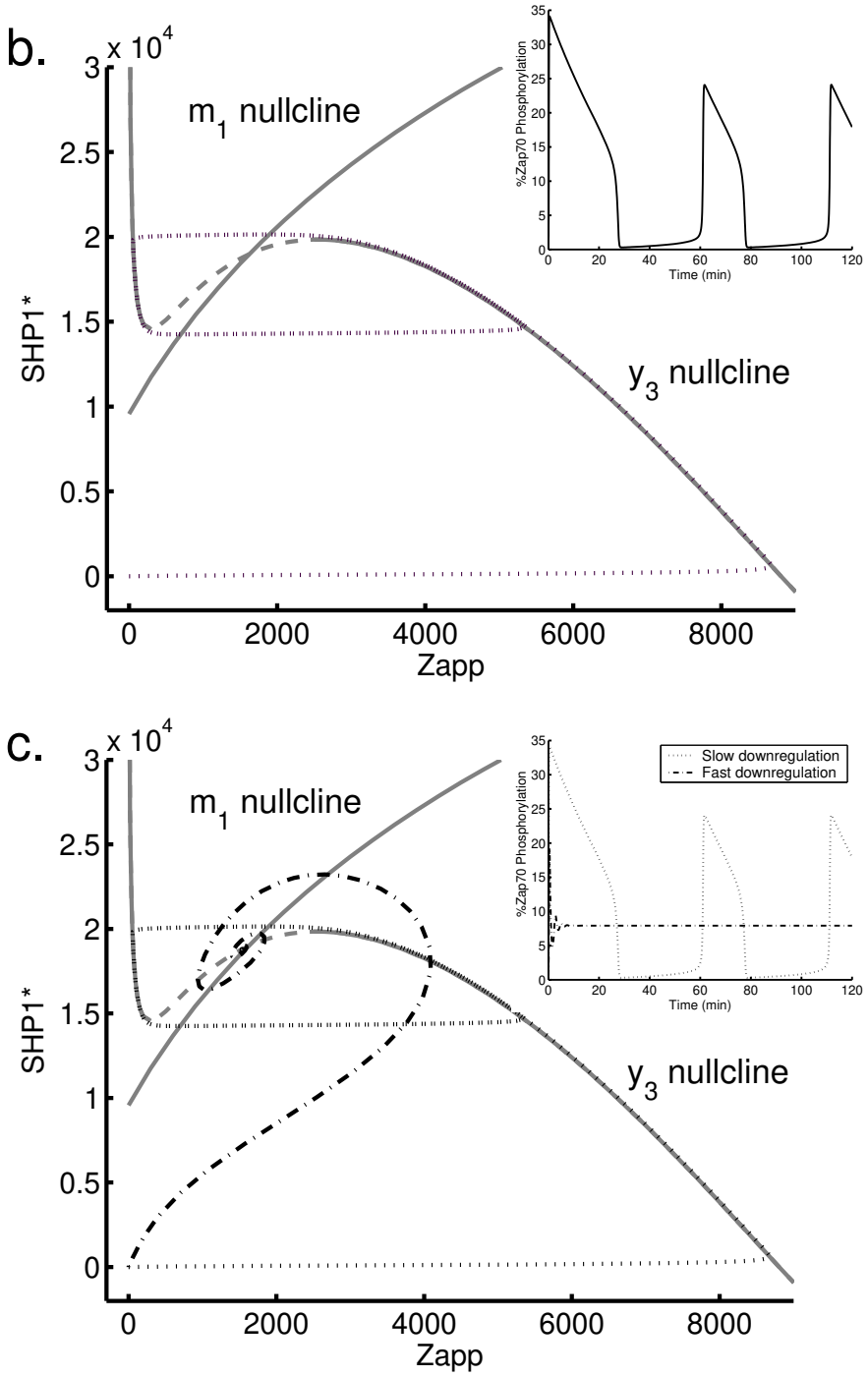

Fig. 8. Results with the reduced 2nd order model. $k_{10,f}$=15e-10 (cell/(#·s)) (K_{10}=3.75e-6 cell/#), $k_{11,f}$=$k_{6,f1}$=0. Other parameters are the same as in Table 3 unless specified. Nullclines are specified by the grey lines and phase plane trajectories correspond to black lines. The dashed region of the y_3 nullcline indicates unstable equilibrium points with parameter values stated above. The insets of the figures show the corresponding time course responses of Zap70 phosphorylated at Y319. (a) α=1; (b) α=3; (c) Comparison between slow (dotted black lines) and fast (dashed-dotted black lines) downregulation rates with α=1. (With fast downregulation rate, both $k_{10,f}$ and $k_{10,r}$ are 100 times the values in Table 3 which corresponds to slow downregulation rate.)

Consistent with the observations on the full order model to fit the experimental data, analysis of the second order model indicates the necessity of a slow signal downregulation rate as compared to signal propagation for appropriate model dynamics. This conclusion was drawn from the observations that the stability of the system and phase plane of the responses is sensitive to the rate of signal downregulation as characterized by $k_{10,f}$. When increasing the rate of downregulation while keeping K_{10} fixed, the nullclines of the system remain the same but the stability of the equilibrium points change. With $\alpha = 1$, the unstable region (dashed portion) completely stabilizes when the rate is increased by 100 fold that gives rise to the transition from an oscillatory to a sustained response as shown in Fig. 8c.

9. Discussion

In this study a detailed kinetic model was developed for the early events in T-cell antigen receptor signaling. This model was explored to extract quantitative information from available experimental data to improve the understanding of the regulatory mechanisms embedded within the pathway. The model was capable of generating damped responses of Zap70 phosphorylation to sustained receptor phosphorylation as consistent with experimental data. To generate this response, the model required an initial rapid cascade of phosphorylation events followed by a comparatively slow downregulation regulated by the negative feedback loops. While the rapid kinetics of kinases renders the ability to overcome the inhibitory effect and produce an overshoot in the response, the slow progression of the negative signal eventually adapt the system to the quiescent state. This difference in the time scales, essential for model reduction as described, has been previously discussed by Grossman and Paul in their

tunable activation threshold theory [20]. Consistent with the finding here, the authors proposed that a rapid, cooperative "excitation"combined with a slow "de-excitation" in the general process of T cell activation gives rise to "excitability", in other word, significant overshooting of the responses.

Current opinion on T-cell activation hypothesizes that it requires the binding duration of the TCR to its ligand be sufficiently long, known as the kinetic proofreading theory [34]. In this work, it is assumed that this binding duration controls the degree of receptor phosphorylation, the model input signal. The developed model predicts that the system responds efficiently only when the input signal is above a certain threshold. Below this level, the system is essentially insensitive to any stimulus. Thus, the thresholding effect enhances TCR specificity and provides sub-threshold noise filtering of the signaling pathway to ensure proper cell response. The importance of such a signaling threshold for T-cell activation may play a role in mediating autoimmune diseases that are characterized by the generation of inappropriate immune responses to self antigens. A decrease in the activation threshold may deteriorate the TCR's ability to differentiate self from foreign antigens, possibly leading to autoimmunity [39]. The importance of the early T-cell signaling events in autoimmune diseases has been implicated in Lck disregulation in T-cells from patients with systemic lupus erythematosus (SLE) [23]. Supporting the importance of thresholding effects in the immune system response, B-cell activation also seems to require a minimum affinity of engaged antibody receptors [35].

As demonstrated, the model exhibits a switch-like behavior and hysteresis with changes in the negative feedback strength. Nonlinear analyses verify the observed effect

arises from the bistable nature of the model as a result of the positive feedback regulation loop residing in the early phase of TCR signaling. Bistability is a common mechanism present in cell signaling systems to achieve ultrasensitivity. This behavior has been most studied within the MAPK (Mitogen-Activated Protein Kinase) signaling pathway. Ferrel and Machleder demonstrated the MAPK pathway in oocytes operates as an on-or-off switch [15] and the detailed MAPK model developed by Bhalla and Iyenger exhibited bistability in the presence of positive feedback loops [5].

Since the positive feedback strength is partially dictated by the relative activity of phospho-Zap70 bound to free active SFK in phosphorylating Zap70, this ratio (α) becomes a critical parameter of the system that determines the type of responses obtainable from the model. While large αs give rise to bistability, smaller αs may produce stable oscillations. Although damped responses are typical for T-cell signaling as the cell has to eventually return to its basal state after the activation, oscillatory behavior may exist as well for short time periods. Existing examples of oscillatory signaling pathway responses include Ca^{2+} signaling [46], cell cycle progression [51], circadian rhythms [30, 50], and possibly the MAPK pathway as shown with some theoretical work [24]. Such oscillatory behaviors not only cause the cell to alternate between different states as in the case of cell cycle progression or circadian rhythms, but also may contribute to frequency modulated signaling processes such as nerve cell Ca^{2+}/calmodulin-dependent kinase II activity [4]. As the current model focuses on the early T-cell signaling events, it is possible that the predicted oscillations may only occur until downstream events exert additional regulations. Some of our experimental results indicate a second rising phase of the ZAP70 phosphorylation, which may progress into an oscillation (Fig.

2). In fact, the observed oscillation type dynamics can be fit well with the full model for a different set of parameter values of which the physiological relevance is under investigation and will need further experimentation to validate. Verification of the ZAP70 phosphorylation oscillations and the associated fitted model parameters will require additional experimental measurements for extended time periods (beyond 120 minutes) with the ability to block all possible effects from downstream signaling pathways (currently a MEK inhibitor is used to block any potential ERK feedback to Lck [49]).

To the best of our knowledge, the current model is the first one that has investigated the role of three known regulatory mechanisms in the early TCR signaling phase in detail: the signal downregulation by SHP-1 activation and CD45 translocation, and signal augmentation through enhanced SFK activity when associated with Zapp. Theoretical analyses in this paper suggest that the interaction of these positive and negative feedback loops leads to interesting system properties such as thresholding and bistability. According to Grossman and Paul's tunable activation threshold theory, the competition between positive and negative feedback loops allows dynamic modulation and adaptation of T cell's responses to hierarchy of ligands [20]. This theory was previously interpreted through the experimental evidence that a positive feedback regulation from the downstream effector Erk that suppresses SHP-1 activity contributes to the differentiation between agonist and antagonist peptide ligands [36, 49]. Here our findings demonstrate that even the top module of the signaling pathway alone encompasses the capability of ligand discrimination through the cooperative and counteracting activities of membrane-proximal protein tyrosine kinases and phosphatases. The importance of such kinase-phosphatase balance in T cell signaling has been supported by experimental

evidence [44].

The presence of multiple feedback regulation loops enabled the model to exhibit a large variety of dynamics with relatively small changes in the parameter values (within an order of magnitude). The feasible set of dynamics include sustained responses, damped responses, stable self-repeating cycles, and others not shown. This diversity of dynamics is not unexpected given the variability found in all biological systems. In *E. coli*, more than 50% cell-cell variation can be found in the gene expression under the lac promoter due to intrinsic noise in biochemical processes [13]. Since the presented experiment results were obtained with populations of T-cells, the variations of individual cell responses were eliminated by averaging. However, the population average and single cell results can differ widely as evidenced by a study of individual oocytes [15]. Although optical interrogation of individual T-cells is feasible for some signaling components such as Ca^{2+}, conducting biochemistry experiments to quantify the response of an individual cell is not yet feasible. Hence the presence of such variability in T-cell signaling needs further experimental confirmation, ideally though single-cell measurements.

The model and approaches presented in this paper can be utilized as a framework to study the contributions of other possible regulatory mechanisms such as protein degradation induced by Cbl [33, 38]. Furthermore, extended models that incorporate downstream as well as costimulatory signaling pathways can be constructed to investigate the cellular control scheme implemented through feedforward and feedback regulations to and from downstream signaling pathways, and signal modulation by pathway crosstalk. Notice that as the scale of the system grows, the simple nonlinear analysis method employed in this paper becomes inefficient and

the usage of professional software such as AUTO is inevitable. When integrated with and validated by available experimental data, these models and analyses will eventually become reliable prediction tools that potentially can be used to design treatments for diseases arising from defects in T-cell signaling pathways.

Acknowledgements

This work is supported in part by National Institutes of Health grants CA37372 and GM48099.

Appendix

This appendix uses conditions $\upsilon_1=\upsilon_2=\upsilon_6=\upsilon_7=\upsilon_8=\upsilon_9=\upsilon_{10}=\upsilon_{11}=0$, $-\upsilon_3=\upsilon_4=\upsilon_5$ and the mass conservation equations in (3) to specify all the rest state variables in the model as functions of the 'basic' variables (y_3, m_1 and r) and derives the equations (4), (5) and (6) in the paper.

As the different species of SFK (x_i, i=0,1,2,3) must satisfy the conservation of mass, $x_0+x_1+x_2+x_3=X_t$, it is possible to write them as fractions of the total (X_t) from $\upsilon_2=0$, $-\upsilon_3=\upsilon_4=\upsilon_5$. This specifies x_0, x_1, x_2 and x_3 in terms of y_3, m_1, and r:

$$\begin{aligned} x_0 &= \frac{\theta}{1+\phi+\varphi+\theta} X_t = \hat{x}_0(y_3, m_1, r) \\ x_1 &= \frac{1}{1+\phi+\varphi+\theta} X_t = \hat{x}_1(y_3, m_1, r) \\ x_2 &= \frac{\phi}{1+\phi+\varphi+\theta} X_t = \hat{x}_2(y_3, m_1, r) \\ x_3 &= \frac{\varphi}{1+\phi+\varphi+\theta} X_t = \hat{x}_3(y_3, m_1, r) \end{aligned} \tag{1a}$$

in which:
$$\begin{cases} \phi = \dfrac{k_{3,f}k_{4,r} + k_{4,f}k_{5,f}y_3 + k_{5,f}k_{3,f}}{k_{5,f}k_{3,r}(m_1) + k_{4,r}k_{5,r}y_3 + k_{4,r}k_{3,r}(m_1)} \\ \varphi = y_3 \dfrac{k_{3,r}(m_1)k_{4,f} + k_{4,f}k_{5,r}y_3 + k_{5,r}k_{3,f}}{k_{5,f}k_{3,r}(m_1) + k_{4,r}k_{5,r}y_3 + k_{4,r}k_{3,r}(m_1)}. \\ \theta = \dfrac{k_{2,r}}{k_{2,f}r} \\ k_{3,r}(m_1) = m_1 k_{3,r1} + k_{3,r2} \end{cases}$$

Conditions $\upsilon 6=\upsilon 7=0$ and the mass conservation of all Csk and Cbp species ($z_0+z_1+v_1=Z_t$, $v_0+v_1=V_t$) define the dependence of w_0 on y_3, m_1, and r (when v_1 is replaced with w_0/r,):

$$\left(\frac{1}{K_7\tilde{K}_6(y_3,m_1,r)}-\frac{1}{r}\right)w_0{}^2+\left(Z_t+V_t+\frac{1}{K_7}\right)w_0-rZ_tV_t=0 \qquad (2a)$$

where $\tilde{K}_6(y_3,m_1,r)=\frac{k_{6,f1}\hat{x}_2(y_3,m_1,r)+k_{6,f2}}{k_{6,r}}, K_7=\frac{k_{f,7}}{k_{r,7}}$

Assume the solution to (2a) gives: $w_0=\hat{w}_0(y_3,m_1,r)$.

The relationship of all the forms of Zap70 (y_i, i=0,1,2,3) can be written in terms of y_3, m_1, and r by simultaneously satisfying υ_1=0, υ_8=0, υ_9=0 and the conservation of mass ($y_0+y_1+y_2+y_3+x_3=Y_t$). From υ_8=0, y_2 can be written in terms of y_1, y_3, m_1, and r, utilizing the relationships in (1a) as:

$$y_2=\frac{(k_{8,f1}x_2+k_{8,f2}x_3)y_1}{m_1k_{8,r1}+k_{8,r2}}\equiv K_8(x_2,x_3,m_1)y_1=\tilde{K}_8(y_3,m_1,r)y_1 \qquad (3a)$$

To satisfy υ_1=0, y_0 is specified in terms of y_1:

$$y_0{}^2+(2u-Y_t)y_0-\frac{k_{1,r}y_1}{k_{1,f}}=0 \qquad (4a)$$

Utilizing the conservation of mass ($y_0+y_1+y_2+y_3+x_3=Y_t$) and (3a), y_1 can be expressed as a function of y_0, y_3, m_1, and r to yield:

$$y_1=\frac{Y_t-y_0-y_3-\hat{x}_3(y_3,m_1,r)}{\tilde{K}_8(y_3,m_1,r)+1} \qquad (5a)$$

Substituting (5a) into (4a) provides a quadratic equation of y_0 for any fixed y_3, m_1 and r:

$$y_0{}^2+\left(2u-Y_t+\frac{k_{1,r}}{(\tilde{K}_8(y_3,m_1,r)+1)k_{1,f}}\right)y_0-\frac{k_{1,r}(Y_t-y_3-\hat{x}_3(y_3,m_1,r))}{(\tilde{K}_8(y_3,m_1,r)+1)k_{1,f}}=0 \qquad (6a)$$

As the amounts of these chemical species must be non-negative, the quadratic equation has only one solution of relevance: its positive root. With the solution of (6a) for y_0 in terms of y_3, m_1 and r, (5a) and (3a) specify y_1 and y_2 as functions of y_3, m_1 and r as well. Let the resultant expression of y_0, y_1 and y_2 be $\hat{y}_0(y_3,m_1,r)$, $\hat{y}_1(y_3,m_1,r)$, $\hat{y}_2(y_3,m_1,r)$,

respectively. To derive for a relationship between y_3, m_1 and r, substitute y_2 with $\hat{y}_2(y_3, m_1, r)$ in the constraint imposed by condition υ_9=0. This yields:

$$\left(y_3 + \hat{y}_2(y_3, m_1, r) + \hat{x}_3(y_3, m_1, r) + \frac{k_{9,f2}}{k_{9,f1}} \hat{x}_2(y_3, m_1, r) + \frac{k_{9,f3}}{k_{9,f1}} \hat{x}_3(y_3, m_1, r) \right) \hat{y}_2(y_3, m_1, r) - \frac{(m_1 k_{9,r1} + k_{9,r2}) y_3}{k_{9,f1}} = 0 \quad (7a)$$

(8a) defines the first relationship between the values of y_3, m_1 and r at equilibrium.

Two additional equations on y_3, m_1, and r come from the conditions υ_{10}=0 and υ_{11}=0, and the mass conservation of SHP-1 (m_i) and CD45 (w_i). Derived from υ_{10}=0 and $m_0+m_1=M_t$, (8a) specifies a relationship between y_3, m_1 and r:

$$M_t - m_1 = \frac{m_1}{K_{10} \hat{x}_2(y_3, m_1, r)}, \text{ where } K_{10}=k_{10,f}/k_{10,r} \quad (8a)$$

Since the solution to (2a) yields w_0 as a function of y_3, m_1, and r: $w_0 = \hat{w}_0(y_3, m_1, r)$, υ_{11}=0 and $w_0+w_1=W_t$ sets the third constraint on y_3, m_1 and r:

$$\hat{w}_0(y_3, m_1, r) = \frac{W_t - \hat{w}_0(y_3, m_1, r)}{K_{11} \hat{x}_2(y_3, m_1, r)}, \text{ where } K_{11}=k_{11,f}/k_{11,r} \quad (9a)$$

(7a), (8a), and (9a) correspond to equations (4), (5) and (6) which define all possible values of y_3, m_1 and r at equilibrium. Using these three values, the equilibrium values for x_is can be derived from (1a), y_is from (3a), (5a), and (6a) and w_0 is determined from (2a), with which v_1 is computed from $r \times w_0$. From the above values, the equilibrium state of z_0 can be solved using υ_7=0 and $z_0+z_1+v_1=Z_t$ as $z_0 = \frac{Z_t - v_1}{1+K_7}$, and those for the rest of the variables (v_0, m_0, w_1 and z_1) are found by direct application of the conservation of mass relationships. Hereby the equilibrium states of the model are fully specified.

References

1. A.K. Abbas, A.H. Lichtman, and J.S. Pober, *Cellular and Molecular Immunology*, *3 ed.* W.B. Saunders Company, 1997, pp. 17.
2. O. Acuto and D. Cantrell, T Cell Activation and the Cytoskeleton, *Annu Rev Immunol* **18** (2000) 165-184.
3. N.G. Agrawal and J.J. Linderman, Mathematical Modeling of Helper T Lymphocyte/Antigen-Presenting Cell Interactions: Analysis of Methods for Modifying Antigen Processing and Presentation, *J Theor Biol* **182** (1996) 487-504.
4. B. Alberts, A. Johnson, J. Lewis, M. Raff, K. Roberts, and P. Walter, *Molecular Biology of the Cell*, *4 ed.* Garland Pub, 2002, pp. 865.
5. U.S. Bhalla, Robustness of the Bistable Behavior of a Biological Signaling Feedback Loop, *Chaos* **11** (2001) 221-226.
6. F.A. Brightman and D.A. Fell, Differential Feedback Regulation of the MAPK Cascade Underlies the Quantitative Differences in EGF and NGF Signalling in PC12 Cells, *FEBS Lett* **482** (2000) 169-174.
7. L.A. Cary and J.A. Cooper, Molecular Switches in Lipid Rafts, *Nature* **404** (2000) 945-947.
8. A.K. Chakrabory, M.L. Dustin, and A.S. Shaw, *In Silico* Models for Cellular and Molecular Immunology: Success, Promises and Challenges, *Nat Immunol* **4** (2003) 933-936.
9. C. Chan, Modeling T Cell Activation, Ph.D. Thesis, Centre for Nonlinear Dynamics and its Applications, University College London, 2002.
10. C. Chan, A.J. George, and J. Stark, Cooperative Enhancement of Specificity in a Lattice of T Cell Receptors., *P Natl Acad Sci USA* **98** (2001) 5758-5763.
11. D. Davidson, M. Bakinowski, M.L. Thomas, V. Horejsi, and A. Veillette, Phosphorylation-Dependent Regulation of T-Cell Activation by PAG/Cbp, a Lipid-Associated Transmembrane Adaptor, *Mol Cell Biol* **23** (2003) 2017-1028.
12. E.J. Doedel, R.C. Paffenroth, A.R. Champneys, T.F. Fairgrieve, Y.A. Kuznetsov, B. Sandstede, et al., *Auto 2000: Continuation and Bifurcation Software for Ordinary Differential Equations (with Homcont)*. 2001, Caltech.
13. M.B. Elowitz, A.J. Levine, E.D. Siggia, and P.S. Swain, Stochastic Gene Expression in a Single Cell, *Science* **297** (2002) 1183-1186.
14. J.R. Faeder, W.S. Hlavacek, I. Reischl, M.L. Blinov, H. Metzger, A. Redondo, et al., Investigation of Early Events in FcεRI-Mediated Signaling Using a Detailed Mathematical Model, *J Immunol* **170** (2003) 3769-3781.
15. J.E. Ferrell and E.M. Machleder, The Biochemical Basis of an All-or-None Cell Fate Switch in Xenopus Oocytes, *Science* **280** (1998) 895-897.
16. B.A. Freiberg, H. Kupfer, W. Maslanik, J. Delli, J. Kappler, D.M. Zaller, et al., Staging and Resetting T Cell Activation in SMACs, *Nat Immunol* **3** (2002) 911-917.
17. G.C. Gary and B.M. Sefton, Specific Dephosphorylation of the Lck Tyrosine Protein Kinase at Tyr-394 by the SHP-1 Protein-Tyrosine Phosphatase, *J Biol Chem* **276** (2001)

23173-23178.
18. R.N. Germain and I. Stefanova, The Dynamics of T Cell Receptor Signaling: Complex Orchestration and the Key Roles of Tempo and Cooperation, *Annu Rev Immunol* **17** (1999) 467-522.
19. R.A. Goldsby, T.J. Kindt, B.A. Osborne, and J. Kuby, *Immunology*, *5 ed.* W.H. Freeman and Company, 2003, pp. 13.
20. Z. Grossman and W.E. Paul, Autoreactivity, Dynamic Tuning and Selectivity - Opinion, *Current Opinion in Immunology* **13** (2001) 687-698.
21. R. Heinrich, B.G. Neel, and T.A. Rapoport, Mathematical Models of Protein Kinase Signal Transduction, *Molecular Cell* **9** (2002) 957-970.
22. W.S. Hlavacek, A. Redondo, C. Wofsy, and B. Goldstein, Kinetic Proofreading in Receptor-Mediated Transduction of Cellular Signals: Receptor Aggregation, Partially Activated Receptors, and Cytosolic Messengers, *B Math Biol* **64** (2002) 887-911.
23. E.C. Jury, P.S. Kabouridis, A. Abba, R.A. Mageed, and D.A. Isenberg, Increased Ubiquitination and Reduced Expression of Lck in T Lymphocytes from Patients with Systemic Lupus Erythematosus, *Arthrit Rheum* **48** (2003) 1343-1354.
24. B.N. Kholodenko, Negative Feedback and Ultrasensitivity Can Bring About Oscillations in the Mitogen-Activated Protein Kinase Cascades, *Eur J Biochem* **267** (2000) 1583-1588.
25. S. Kim, S.M. Patrick, N.S. Braunstein, J.L. Thomas, and E.F. Leonard, Modeling of Early Events in T Cell Signal Transduction after Controlled T Cell Activation by Peptide Major Histocompatibility Complex, *Ann Biomed Eng* **29** (2001) 373-383.
26. M.E. Labadia, S. Jakes, C.A. Grygon, D.J. Greenwood, J. Schembri-King, S.M. Lukas, et al., Interaction between the SH2 Domains of ZAP-70 and the Tyrosine-Based Activation Motif 1 Sequence of the ζ Subunit of the T-Cell Receptor, *Arch Biochem Biophys* **342** (1997) 117-125.
27. K.H. Lee, A.R. Dinner, C. Tu, G. Campi, S. Raychaudhuri, R. Varma, et al., The Immunological Synapse Balances T Cell Signaling and Degradation, *Science* **302** (2003) 1218-1222.
28. S.J. Lee, Y. Hori, J.T. Groves, M.L. Dustin, and A.K. Chakrabory, Correlation of a Dynamic Model for Immunological Synapse Formation with Effector Functions: Two Pathways to Synapse Formation, *Trends Immunol* **23** (2002) 492-499.
29. S.J. Lee, Y. Hori, J.T. Groves, M.L. Dustin, and A.K. Chakrabory, The Synapse Assembly Model, *Trends Immunol* **23** (2002) 500-502.
30. J.C. Leloup and A. Goldbeter, Chaos and Birhythmicity in a Model for Circadian Oscillations of the PER and TIM Proteins in Drosophila, *J Theor Biol* **198** (1999) 445-459.
31. A. Leo and B. Schraven, Adaptors in Lymphocyte Signaling, *Curr Opin Immunol* **13** (2001) 307-316.
32. G.M. Lord, R.I. Lechler, and A.J. George, A Kinetic Differentiation Model for the Action of Altered TCR Ligands, *Immunol Today* **20** (1999) 33-39.
33. M.P. Loreto, D.M. Berry, and C.J. McGlade, Functional Cooperation between c-Cbl and Src-Like Adaptor Protein 2 in the Negative Regulation of T-Cell Receptor

Signaling, *Mol. Cell. Biol.* **22** (2002) 4241-4255.
34. T.W. McKeithan, Kinetic Proofreading in T-Cell Receptor Signal Transduction, *P Natl Acad Sci USA* **92** (1995) 5042-5046.
35. P.K.A. Mongini, C.A. Blessinger, and J.P. Dalton, Affinity Requirements for Induction of Sequential Phases of Human B Cell Activation by Membrane IgM-Cross-Linking Ligands, *J Immunol* **146** (1991) 1791-1800.
36. D.L. Mueller, Tuning the Immune System: Competing Positive and Negative Feedback Loops, *Nature Immunology* **4** (2003) 210-211.
37. T. Mustelin, R.T. Abraham, C.E. Rudd, A. Alonso, and J.J. Merlo, Protein Tyrosine Phosphorylation in T Cell Signaling, *Front Biosci* **7** (2002) d918-d969.
38. M. Naramura, I. Jang, H. Kole, F. Huang, D. Haines, and H. Gu, c-Cbl and Cbl-b Regulate T Cell Responsiveness by Promoting Ligand-Induced TCR Down-Modulation, *Nat Immunol* **3** (2002) 1192-1199.
39. P.S. Ohashi, T-Cell Signaling and Autoimmunity: Molecular Mechanisms of Disease, *Nat Rev Immunol* **2** (2002) 427-438.
40. M.W. Olszowy, P.L. Leuchtmann, and A. Veillette, Comparison of p56lck and p59fyn Protein Expression in Thymocyte Subsets, Peripheral T Cells, NK Cells, and Lymphoid Cell Lines, *J Immunol* **155** (1995) 4236-4240.
41. E.A. Ottinger, M.C. Botfield, and S.E. Shoelson, Tandem SH2 Domains Confer High Specificity in Tyrosine Kinase Signaling, *J Biol Chem* **273** (1998) 729-735.
42. M. Pelosi, V.D. Bartolo, V. Mounier, D. Mege, J.M. Pascussi, E. Dufour, et al., Tyrosine 319 in the Interdomain B of ZAP-70 Is a Binding Site for the Src Homology 2 Domain of Lck, *J Biol Chem* **274** (1999) 14229-14237.
43. J.D. Rabinowitz, C. Beeson, D.S. Lyons, M.M. Davis, and H.M. McConnell, Kinetic Discrimination in T-Cell Activation, *P Natl Acad Sci USA* **93** (1996) 1401-1405.
44. A.E. Schade and A.D. Levine, Phosphatases in Concert with Kinases Set the Gain for Signal Transduction through the T Cell Receptor, *Molecular Immunology* **40** (2003) 531-537.
45. B. Schoeberl, C. Eichler-Jonsson, E.D. Gilles, and G. Muller, Computational Modeling of the Dynamics of the MAP Kinase Cascade Activated by Surface and Internalized EGF Receptors, *Nat Biotechnol* **20** (2002) 370-375.
46. G.D. Smith, R.J. Lee, J.M. Oliver, and J. Keizer, Effect of Ca^{2+} Influx on Intracellular Free Ca^{2+} Responses in Antigen-Stimulated RBL-2H3 Cells, *Am J Physiol Cell Physiol* **270** (1996) 939-952.
47. E. Sontag, Structure and Stability of Certain Chemical Networks and Applications to the Kinetic Proofreading Model of T-Cell Receptor Signal Transduction, *IEEE T Automat Contr* **46** (2001) 1028-1047.
48. J. Sousa and J. Carneiro, A Mathematical Analysis of TCR Serial Triggering and Down-Regulation, *Eur J Immunol* **30** (2000) 3219-3227.
49. I. Stefanova, B. Hemmer, M. Vergelli, R. Martin, W.E. Biddison, and R.N. Germain, TCR Ligand Discrimination Is Enforced by Competing Erk Positive and SHP-1 Negative Feedback Pathways, *Nat Immunol* **4** (2003) 248-254.
50. J.J. Tyson, C.I. Hong, C.D. Thron, and B. Novak, A Simple Model of Circadian

Rhythms Based on Dimerization and Proteolysis of PER and TIM, *Biophys J* **77** (1999) 2411-2417.

51. J.J. Tyson and B. Novak, Regulation of the Eukaryotic Cell Cycle: Molecular Antagonism, Hysteresis, and Irreversible Transitions, *J Theor Biol* **210** (2001) 249-263.
52. A. Veillette, S. Latour, and D. Davidson, Negative Regulation of Immunoreceptor Signaling, *Annu Rev Immunol* **20** (2002) 669-707.
53. C. Wofsy, D. Coombs, and B. Goldstein, Calculations Show Substantial Serial Engagement of T Cell Receptors, *Biophys J* **80** (2001) 606-612.